Localization of Interaction using Fibre-Optic Shape Sensing in Soft-Robotic Surgery Tools*

Solène Dietsch**, Aoife McDonald-Bowyer**, Emmanouil Dimitrakakis, Joanna M. Coote, Lukas Lindenroth, Agostino Stilli, Danail Stoyanov

***Abstract*— Minimally invasive surgery requires real-time tool tracking to guide the surgeon where depth perception and visual occlusion present navigational challenges. Although vision-based and external sensor-based tracking methods exist, fibre-optic sensing can overcome their limitations as they can be integrated directly into the device, are biocompatible, small, robust and geometrically versatile. In this paper, we integrate a fibre Bragg grating-based shape sensor into a soft robotic device. The soft robot is the pneumatically attachable flexible (PAF) rail designed to act as a soft interface between manipulation tools and intra-operative imaging devices. We demonstrate that the shape sensing fibre can detect the location of the tools paired with the PAF rail, by exploiting the change in curvature sensed by the fibre when a strain is applied to it. We then validate this with a series of grasping tasks and continuous US swipes, using the system to detect in real-time the location of the tools interacting with the PAF rail. The overall location-sensing accuracy of the system is 64.6%, with a margin of error between predicted location and actual location of 3.75 mm.**

I. INTRODUCTION

Minimally invasive surgery (MIS) is becoming the gold standard for many surgical procedures. However, there are long training times due to the steep learning curve associated with working in an environment with a limited field of view and limited perception of depth and scene shape [1][2]. Robotic-assisted laparoscopic surgery, although offering better instrument manoeuvrability and increased degrees of freedom (DoF), suffers from visual and sensory occlusion to the surgical workspace through the endoscopic field of view (FoV) [3].

Surgical tool tracking technology assists the surgeon in guiding them during robotic-assisted surgical procedures by estimating the pose of surgical tools with respect to the anatomy in the endoscopic FoV[4]. The most common approaches to tool-tracking in surgery are vision-based [5][6], including marker and marker-less tracking [7], intra-operative imaging such as Ultrasound (US) [8] and Fluoroscopy [9], and pre-operative imaging such as Computed Tomography (CT) [10] and Magnetic Resonance Imaging (MRI) [11].

Image-based marker-less tracking can prove beneficial to tool-tracking by providing positional and motion information without modification to the tool itself. However, the challenge of visual occlusion remains, as well as robustness due to the vast array of different surgical tools available and the patient-specific surgical workspace [7]. Other limitations of purely vision-based tracking are discussed extensively in [12], namely reliance of segmentation accuracy performance on instrument colour, lack of distinct feature points in the surgical workspace [13], and dependency on the direct line of sight [14].

Alternative forms of tool tracking are: electromagnetic (EM) [15][16][17], optical [18], and robot kinematics [19]. Electromagnetic tracking has been used for localizing devices in situations where direct line-of-site is unavailable [20], such as in endoscopic capsules [21], orthopaedic surgery [22], and in combination with ArUco markers for tracking intra-operative US probes [23]. Kinematics-based localization has traditionally been employed for continuum robots [24] but has been demonstrated in combination with vision [25] and marker-based tracking [26] in the surgical setting.

A potentially beneficial method of tool-tracking in MIS is fibre-optic sensing (FOS). FOS is ideal for this application as sensors can be fabricated on small scales, are flexible, bio-compatible, and immune to electromagnetic interference [27]. FOS has many advantages over other tool tracking methods in this context. It is not susceptible to local field distortions, unlike EM tracking, where the use of a C-arm in theatre can introduce errors on the millimetre scale [28]. It also is not heavily reliant on image quality, segmentation ability, and line-of-sight as in vision-based methods [3][7]. Intensity-modulated optical fibres have been used to estimate curvature in orthopaedic systems [29], while the pose of a soft actuator was estimated using a braided configuration of optical sensors [30]. Fibre-optic ultrasound sensors have also been employed in ultrasonic needle-tracking [31].

The use of fibre optic sensors based on Fibre Bragg Gratings (FBG) has been widely investigated in medical robotics for shape sensing and tool tracking [31][32][33][34]. In [35], the authors present a novel FBG-based sensor to localize tissue abnormalities in MIS. The sensor outperformed previous work in measuring the force applied to a tissue phantom and demonstrated how FBG-based sensing of force distribution can be used to locate tumours. Further

*This research was funded in whole, or in part, by the Wellcome/EPSRC Centre for Interventional and Surgical Sciences (WEISS) [203145/Z/16/Z]; the Engineering and Physical Sciences Research Council (EPSRC) [EP/P027938/1, EP/R004080/1, EP/P012841/1]; and the Royal Academy of Engineering Chair in Emerging Technologies Scheme [CiET1819/2/36]. (Corresponding author: Agostino Stilli, e-mail: a.stilli@ucl.ac.uk)

All the authors are with the Wellcome/EPSRC Centre for Interventional and Surgical Sciences, University College London, London W1W 7EJ, U.K.

**These authors equally contributed to this work

This research was funded in whole, or in part, by the Wellcome/EPSRC Centre for Interventional and Surgical Sciences (WEISS) [203145/Z/16/Z]; the Engineering and Physical Sciences Research Council (EPSRC) [EP/P027938/1, EP/R004080/1, EP/P012841/1]; and the Royal Academy of Engineering Chair in Emerging Technologies Scheme [CiET1819/2/36].
For the purpose of open access, the author has applied a CC BY public copyright licence to any author accepted manuscript version arising from this submission.

experiments were conducted by [36] on ex-vivo organs, and force distribution maps were used to localize tumours with better accuracy and lower palpation forces than conventional sensors. FBG-based sensing has also been used in retinal surgery, where the forces involved are below the level of human perception [33], and in endovascular surgery, where sensors are required to operate on the micro-scale [34].

FBG-based sensing lends itself well to the field of soft robotics, as the sensors are able to bend and contort themselves in the same manner as many soft robotic devices. Soft robots are ideally suited to laparoscopic surgical applications as soft tissue is deformable and the surgical environment is highly dynamic [12]. The use of soft robotics in minimally invasive and robotic-assisted laparoscopic surgery has garnered much attention in recent years due to their compliance with these complex environments while presenting a significantly lower risk of trauma than conventional rigid instruments [37]. However, the dynamism of the surgical workspace coupled with the challenges of soft robotic control adds further complexity to tracking problems [12].

In previous work, we presented a Pneumatically Attachable Flexible [38] (PAF) rail to be deployed in Robotic Assisted Partial Nephrectomy (RAPN) for the facilitation of the US scanning sub-task. The proposed use and deployment process of the PAF rails in RAPN is fully detailed in [38]. The purpose of the PAF rail system is to act as a soft interface between rigid tools and organs targeted in the context of manipulation tasks, as well as to provide a stable track-like interface to guide probes and tools on the surface where the system is deployed, e.g. in the case of ultrasound (US) scanning with drop-in US probes during intra-operative image acquisition [39]. In this work, we demonstrate how the sensorised PAF rail can be used to localize pairing tools that would enable real-time tracking of the paired US probe. We employ a first-generation da Vinci Surgical System (Intuitive Surgical Inc., Sunnyvale, CA, US) in combination with the da Vinci Research Kit (dVRK) to test how well the location of grasping can be identified based on the curvature information derived from the shape sensing fibre embedded in the PAF rail system. We further demonstrate that the sensing framework can be applied to pairing the US probe with the rail and tracking the location of the probe with respect to the rail. In the clinical environment, this allows positional information, as well as cues for when the US probe or grasping tool has detached, to be relayed back to the surgeon.

The paper is structured as follows; in Section II, the design and fabrication of the sensorised PAF rails with embedded FBG sensors is described, as well as the experimental setup involving the da Vinci Surgical System and dVRK. Section III covers experimental results of the curvature sensing and tool localization experiments; these results are discussed in the context of robotic-assisted minimally invasive surgery. Finally, Section V concludes this paper and provides direction for further work.

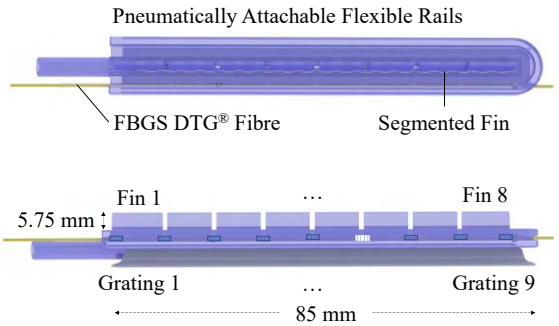

Fig. 1. Schematic diagram of the PAF rail with integrated FBGS DTG shape-sensing fibre. The top view (top) shows the segmented grasping fin running centrally along the axis of the rail. The side view (bottom) highlights how each individual FBG sensor is positioned with respect to the fins.

II. MATERIAL AND METHODS

A. Design and Fabrication of the Sensorised PAF rails

The design and fabrication techniques of the PAF rails was introduced in [38]. In this study, the proposed design improves on the rail-tool interface by introducing a continuous segmented fin that enables grasping of the rail at any point along it, while maintaining axial flexibility (see Fig. 1). The PAF rail is fabricated using injection moulding of Smooth-Sil 940™ silicone (Smooth-On Inc., Macungie, PA, US). To facilitate curvature sensing, a shape sensing optical fibre is inserted in the perimeter of the rail (see Fig. 1). The fibre is threaded through a fine bore low-density polyethylene (LDPE) tube, which is fixed at the proximal end using Sil-Poxy ™ silicone adhesive (Smooth-On Inc., Macungie, PA, US). The shape-sensing fibre is inserted such that each grating pair corresponds to a segment of the fin (see Fig. 1). FBG-based optical sensing utilises the principle of Bragg reflection to facilitate strain and temperature sensing. The fibre in use is a custom-made multi-core fibre (MCF) (CP-FBG DTG® (Draw Tower Grating), FBGS International, Jena, Germany), with a central core surrounded by six equally spaced outer cores. Each core contains 25 FBGs spaced at 10 mm intervals along the optical axis, giving an overall sensing length of 240 mm.

The bending of the shape-sensing fibre induces a specific

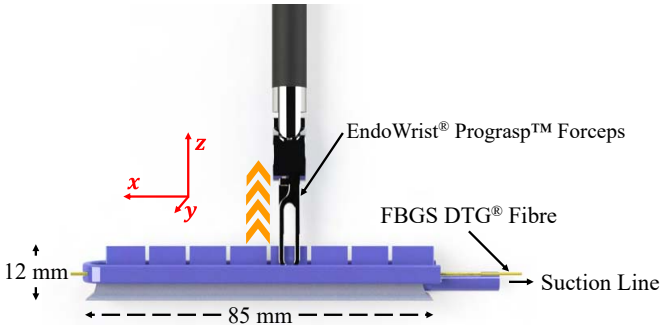

Fig. 2. Schematic diagram of the setup for experiment 2 (side view). The rail is pulled in the $+z$ direction at each fin segment, as highlighted by the orange arrow.

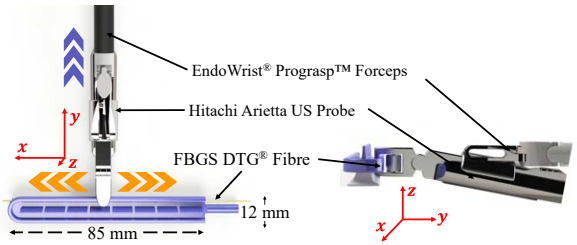

Fig. 3. Schematic diagram of the setup for calibration and experiment 3 (Top view). The Hitachi Arietta drop-in US probe is equipped with a custom attachment, paired with the EndoWrist® ProGrasp™ Forceps during calibration and a hand-held laparoscopic grasping tool during experiment 3. The custom attachment is then manually paired with the perimeter of the rail on the FBGS-embedded side. The coloured arrows indicate the direction of the motion. (Purple) Calibration - The rail is pulled in the +y direction at each fin segment by the US probe. (Orange) Experiment 2 - The US probe slides along the rail in the x direction.

strain in each of the FBGs, which is quantified by shifts in the Bragg wavelengths of the gratings. This is monitored by an optical interrogator, where the raw wavelength shifts are converted to strains for each grating. The strains of the seven gratings at each position along the fibre are then used to compute the local curvature at that position, while the core fibre is used for temperature compensation. A proprietary software (IllumiSense v3.1.x, FBGS International, Jena, Germany) records each core's wavelength data. Then, a proprietary LabVIEW VI (National Instruments, Austin, TX, USA) estimate the curvature along the fibre using these wavelengths as input. Finally, the curvature data is recorded and visualised through a custom Python application.

For our experiments, we employed the first-generation da Vinci robot coupled with the dVRK platform [40], [41]. The PAF rail was suctioned to a platform of acrylic plastic by means of a pneumatic circuit. We used a 3 CFM single-stage vacuum pump (Bacoeng, Hawthorne, CA) to vacuumise a 12-litres vacuum chamber (Bacoeng, Hawthorne, CA) and monitored the pressure with an embedded manometer. The vacuum pressure used for all the tests was $P_{abs} = 7.325$kPa, as discussed in [38]. The chamber was connected with a pressure line to the PAF rail. Each experiment was repeated five times unless otherwise stated.

B. Calibrating the system for Tool Localization

The aim of our first experimental procedure was to obtain a dataset of curvature measurements from the integrated shape-sensing fibre for specific tool-rail interactions. We wanted to measure the robotic end-effector vertical displacement in Cartesian space, at which the sensorised PAF rail could detect the interaction between the grasper and its fins. This trajectory was chosen to replicate the grasping action performed in RAPN. We equipped the first da Vinci Patient Side Manipulator (PSM1) with the EndoWrist® Prograsp™ Forceps. The EndoWrist® ProGrasp™ Forceps were manually paired with the PAF rails by grasping the centre of each fin along the z-axis, perpendicular to the principal axis of the rails (shown in Fig. 2). The fin was then pulled by the grasper tool perpendicularly to the plane locally tangent to the surface of the surface underneath in increments of 1 mm, to a maximum displacement of 7 mm. At each increment, raw wavelength shift and curvature data received from the shape sensing fibre was recorded. The entire trajectory was repeated five times for each of the eight fins. Based on these calibration experiments, the location of the grasping fins was approximated by finding the location, with respect to the length of the rail, of the weighted average of the maximum and minimum of the curvature differential.

Continuing our experimental evaluation, we aimed to calculate the horizontal displacement in Cartesian space, at which the sensorised PAF rails could identify the US probe paired with the rail. We equipped the first da Vinci Patient Side Manipulator (PSM1) with the EndoWrist® Prograsp™ Forceps paired with the drop-in US probe BK X12C4 (BK-Medical Holding Inc., Peabody, Massachusetts), as shown in Fig. 3. The US probe was manually paired with the PAF rails (see Fig. 3). Beginning at the proximal end, the US probe was then pulled in the direction orthogonal to the principal axis of the PAF rails (the y-axis - see Fig. 3) in increments of 1 mm to a maximum displacement of 7 mm. The US probe was then manually slid along the rail to the next fin-adjacent subsection, and the pulling was repeated. This process was repeated five times for each of the eight sub-sections. For each iteration, raw wavelength shift and curvature data received from the FBGS software was recorded.

C. Validation

As a means to validate the sensed locations of the fins, we executed repeated pulling trajectories with the da Vinci Surgical System equipped with the EndoWrist® Prograsp™ Forceps in the same configuration as Fig. 2. Each fin was pulled in the $+z$ direction in one continuous trajectory to a maximum displacement of 5 mm. Raw wavelength and curvature data were recorded at the maximum displacement. The final step in our experimental procedure was to extend the US pairing experiment by sliding the US probe along the rail instead of discrete measurements. We wanted to further test the compatibility of the system with different tools, hence the use of a second intra-operative US probe and hand-held grasper configuration. We paired the Hitachi Arietta drop-in US probe (Hitachi, Chiyoda City, Tokyo, Japan) with a hand-held laparoscopic grasper tool (Ruihui Electronic Technology Co. Ltd., Zhengzhou, China). The attachment was equipped with a custom roller part that pairs with the perimeter of the rail, as shown in Fig. 3. A manual swipe along the length of the rail was executed ten times, five in the $+x$ direction and five in the $-x$ direction. Raw wavelength and curvature data were recorded for the duration of the swipe. We created an animation to visualize in real-time the grasped fin and hence location along the length of the PAF rail, of the probe as it executes the swipe.

III. RESULTS & DISCUSSION

We present in Fig. 4 the evolution of the curvature shift sensed by the rail for incremental pulling displacement on

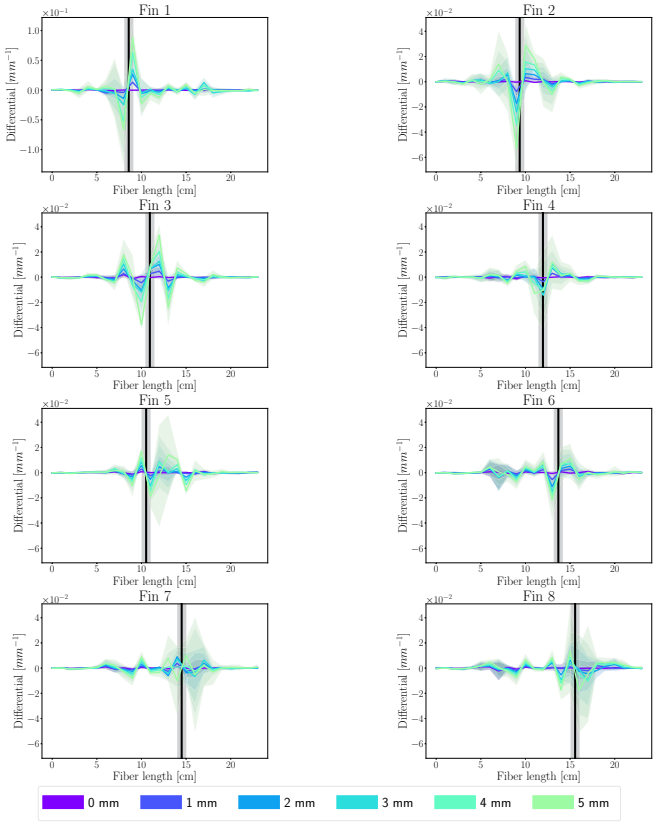

Fig. 4. Experiment 2 results. Each subfigure corresponds to data from each of the 8 fins. The region from x mm to y mm is embedded in the PAF rails. The vertical black lines correspond to the location of pulling based on the weighted average of the maximum and minimum peaks. Note the change in y axis scale.

each of the eight fins. We easily identify the increase in magnitude sensed curvature change at greater displacement, as well as the evolution of the waveform along the length of the fibre as consecutive fins, are pulled.

For each of the grasping fins, we evaluated the relationship between pulling displacement and the absolute change in sensed curvature (see Fig. 5 (right)). We observe a linear relationship between the displacement of the grasper and the shift in absolute curvature. Hence, we observe a relationship between the stretching of the silicone fin and the change in curvature sensed by the shape-sensing fibre embedded in the rail. The magnitude of the curvature differential for fin 1 is greater than the others as fin 1 is adjacent to the pipeline of the PAF rail. At this location, the fin experiences more strain as it is less supported by the surrounding rail structure.

$$a = \frac{|max_{peak}|}{|min_{peak}| + |max_{peak}|} \tag{1}$$

$$b = 1 - a = \frac{|min_{peak}|}{|min_{peak}| + |max_{peak}|} \tag{2}$$

$$m = a.argmax_{peak} + b.argmin_{peak} \tag{3}$$

With $|max_{peak}|$ and $|min_{peak}|$ being the absolute values of the maximum and minimum peaks, respectively. In Fig. 4,

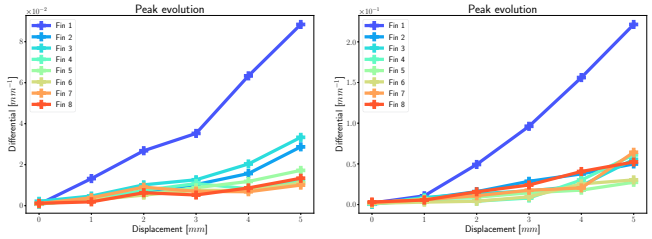

Fig. 5. Pulling displacement (x-axis) against derivative of curvature with respect to distance along the rail for each of the fins. Calibration data from the vertical pulling (left) and from the horizontal pulling (right).

the location of the grasped fin was estimated by calculating the weighted average positions of the maximum peak ($argmax_{peak}$) and minimum peak ($argmin_{peak}$) of curvature differential, as summarised in Eq. 1 Eq. 2 Eq. 3 and as shown in Fig. 8. We represented the sensed grasping position by the black line in each plot, while the shaded region represents the fin width.

We wanted to evaluate the minimum required displacement to obtain an accurate estimate of the fins' position. The main source of error is noise in our system. Thus, we expected to improve our location-sensing accuracy by applying a greater pulling force. In this regard, we display the distance to the sensed location for each fin at a pulling displacement in fig. 6. Overall, the distance to the estimation position at 5mm is less than 2cm for all the fins except for fin 7. In this context, we can expect a good location estimation even when the system undergoes smaller strain.

Fig. 8 (top) shows the derived fin locations for the length of the PAF rail (x-axis) at 5mm displacement. For this task, the derived location of the fins is not sorted correctly. We attribute this to significant noise in the system causing peaks in the sensed curvature signal that does not correspond to a pulling location. Since the signal is dependent on the initial reference wavelength, any initial strain on the rail will introduce peaks that don't correspond to a pulling location. Another source of error comes from the fact that we imply the location of the gratings in respect to the fins. We know the position of the first grating and that they are equally spaced at 10 mm increments along the length of the fibre, but cannot

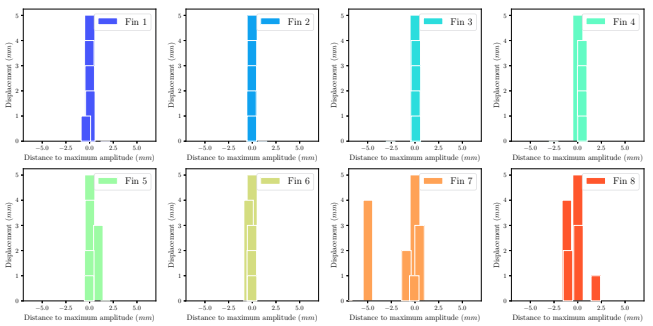

Fig. 6. Distribution of the fin's sensed locations relative to the sensed position at the maximum displacement's amplitude (5mm) according to the displacement amplitude of the grasper.

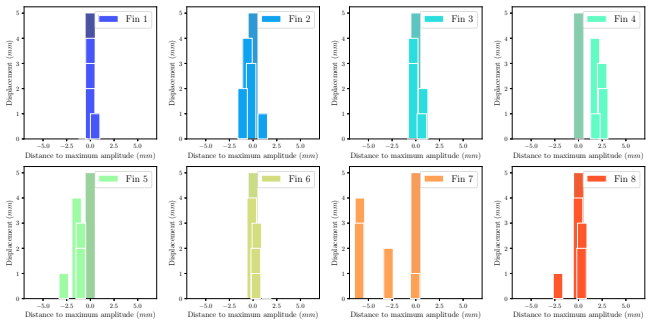

Fig. 7. Distribution of the fin's sensed locations relative to the sensed position at the maximum displacement's amplitude (5*mm*) according to the displacement amplitude of the US probe.

be more specific than that. Moreover, the standard deviation (shaded area of Fig. 4 increases with each subsequent fin pulling. We attribute this result to the error induced by the manual reposition of the grasper on each fin between each experimental iteration. During each iteration, the tool grasps the fin at a different position. Furthermore, the fins themselves are not all the same width in the x direction; fin 1 is 10 mm, fin 8 is 9. 4 mm while the rest are 9 mm.

Results from the horizontal pulling with the paired US probe are shown in Figs. 5 (right), 7, 8 and 9. For each pulling location we evaluated the relationship between pulling displacement and change in sensed curvature (see Fig. 5 (right)). We observed a linear relationship between the pulling displacement perpendicular to the principle axis of the rail and Δcurvature. As highlighted in Fig. 5 (right), Δcurvature is proportional to the $+y$ displacement (see Fig. 3), therefore greater locating accuracy is present at greater displacements. However, Fig. 9 also highlights that a Δcurvature is observable at displacements as small as 1 mm from the axis of the rail. The location of the grasping fin was estimated by the same method as the previous experiment, and is shown in Fig. 8 (bottom). Compared with those estimated by the vertical pulling (top), the fin order is more accurate, at least for the first four fins of the rail. Again, we attribute the error in estimation to noise in the signal causing the peaks selected for location estimation to be incorrect. This could be mitigated in future work by implementing a more robust peak selection algorithm and filtering out the noise. Based on the findings in Fig. 8, we chose to use

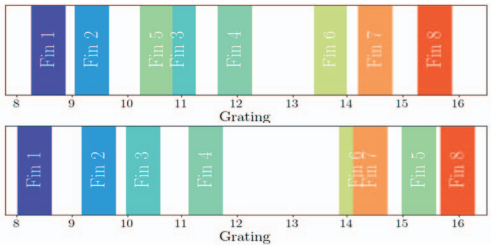

Fig. 8. Derived location of fins along the fibre based on vertical pulling of the fins (top) and horizontal pulling with the US probe (bottom).

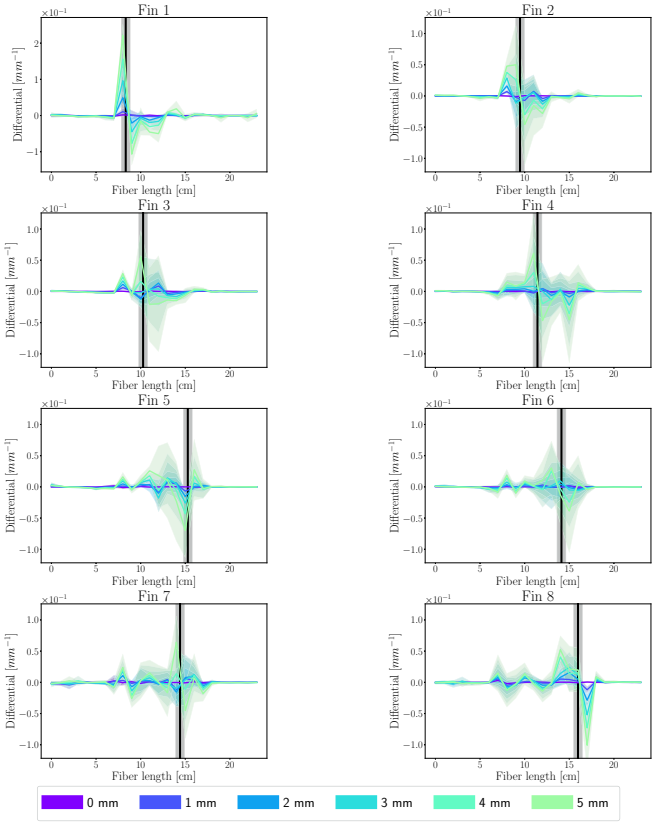

Fig. 9. Experiment 3 results. Each subfigure corresponds to data from each pulling location adjacent to each of the 8 fins. The region from x mm to y mm is embedded in the PAF rails. The vertical black lines correspond to the location of pulling based on the weighted average of the maximum and minimum peaks. Note the change in y axis scale

the model data from the horizontal pulling experiments as that localized the fins in the correct order. In addition, we chose to only select the first and last fin location, as the intermediate fin locations could then be calculated based on prior knowledge of the design of the PAF rail.

A. *Validation Results*

We validated the approximation of grasping locations by performing a second set of grasping tasks to obtain the validation data. We compared the curvature change sensed during validation to the calibration set and reported the results in Fig. 10. Overall sensing accuracy is 64.6 % with the average absolute error in location between actual fin and predicted fin being 3.75 mm, considering an average fin length of 9.18 mm. This represents a 3.6 % error over the entire length of the rail (88.3 mm). The grasping location error is lowest at the 1st and 2nd fin-pair, as well as the 7th and 8th, which are located at opposite ends of the PAF rail. In the centre of the rail, where fins 3 - 6 are located, sensing performance is less accurate. This can be possibly attributed to erroneous sensing of the fin adjacent to the correct one. We could increase accuracy by obtaining more data; we could increase the calibration dataset by sensing grasping at different locations along each fin.

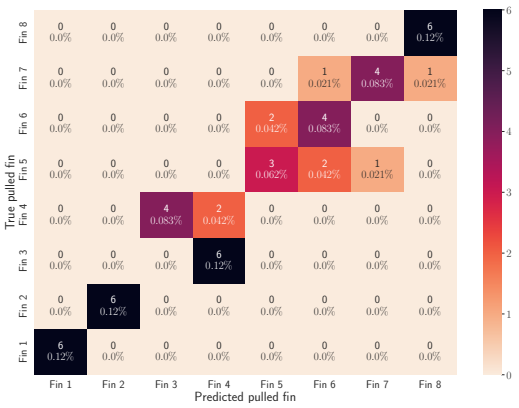

Fig. 10. Confusion matrix of validation set of fin pulling tasks vs. calibration set of fin pulling tasks.

The continuous US swipe was used to validate the pulling data obtained in experiments described in II.B. As the swipe was executed, our custom graphical user interface (GUI) provided real-time visualisation of which fin was adjacent to the US probe. This is done by highlighting in block colour the fin being detected. It also provided visualisation of the sensed curvature derivative, with applied noise thresholding. Snapshots of this task executed in the real frame vs the sensing GUI are shown in Fig. 11 for three example locations. At all three locations, it can be seen on the GUI that the fin adjacent to the US probe has been correctly identified.

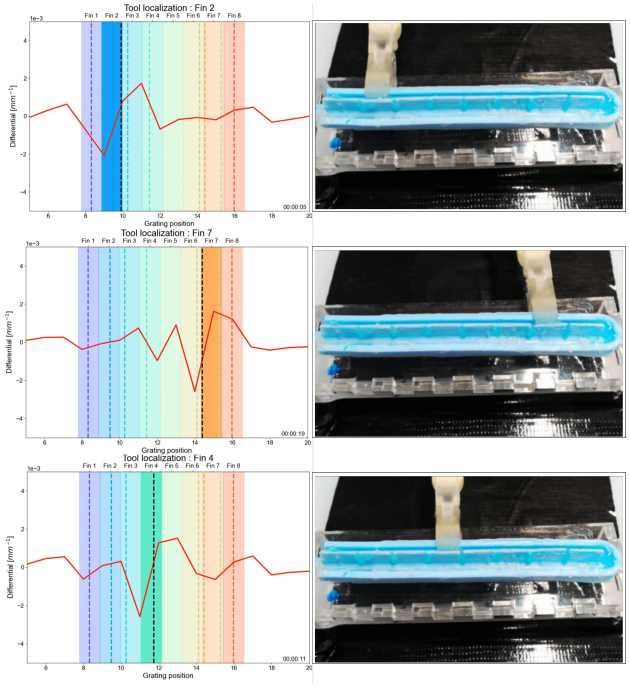

Fig. 11. Snapshots of the US probe sliding execution in the sensed location GUI (left) and from the video stream (right). The custom GUI signifies the detected fin with a solid colour block. The real-time curvature differential is also visualised. We display three random samples of the sliding acquisition; in each case, we correctly detected the fin adjacent to the US probe, as determined by visual inspection.

IV. CONCLUSION

This paper presented an integrated system for localizing tools during grasping and interaction with the PAF rail using fibre-optic shape sensing. Sensing the tools' location paired with the PAF rail in real-time is highly beneficial for use in surgical environments where image-based and EM tracking is not possible.

A multi-core FBG optical fibre was embedded in the body of the PAF device and uses local wavelength shift to sense curvature along the axis of the rails, therefore providing information on local curvature changes without the need for external sensors. We exploited this capacity to sense a curvature shift to provide positional information on surgical tools paired with the PAF rail.

Our paper demonstrates the capability of FBG sensors embedded in a soft-robotic device to detect the location of pairing tools. To confirm this idea, two different task tests, grasping and pairing with the US probe, were conducted using a first-generation da Vinci surgical robot with the dVRK. The curvature data from these experiments helped determine the location of grasping, by finding the point long the rail where the derivative of curvature was a maximum/minimum. This was then validated by performing a series of grasping tasks on the fins and a continuous swipe with a paired US probe. Using the prior localization information we were able to detect which fin was interacting with a tool with a 64.6% success rate and determine the location of the probe in real-time as it moves along the length of the rail.

Future work will focus on addressing the current limitations of the system; increasing the volume of calibration data available, and looking into noise filtering and different peak detection algorithms. We will need to ascertain the sensitivity of the system, to find the minimum interaction with the PAF rail needed to correctly detect the location of the interaction. Beyond this, we would like to assess how well the proposed system can perform in detecting when pairing tools have become detached, as this will provide useful information to the surgeon. Nonetheless, one key drawback of FBG sensing technology is its high cost, particularly when compared with the cost of devices they are integrated into [42]. Sterilization, robustness and single-use are important issues that currently provide barriers to translating this device to surgery. However, the system's sensitivity provides a benchmark for evaluating future shape-sensing modalities in this context.

REFERENCES

[1] V. Vitiello, S. L. Lee, T. P. Cundy, and G. Z. Yang, "Emerging robotic platforms for minimally invasive surgery," vol. 6, pp. 111–126, 2013.

[2] S. L. Lee, M. Lerotic, V. Vitiello, S. Giannarou, K. W. Kwok, M. Visentini-Scarzanella, and G. Z. Yang, "From medical images to minimally invasive intervention: Computer assistance for robotic surgery," *Computerized Medical Imaging and Graphics*, vol. 34, pp. 33–45, 1 2010.

[3] T. G. Manning, M. Perera, D. Christidis, N. Kinnear, S. McGrath, R. O'Beirne, P. Zotov, D. Bolton, and N. Lawrentschuk, "Visual Occlusion During Minimally Invasive Surgery: A Contemporary Review of Methods to Reduce Laparoscopic and Robotic Lens Fogging and Other Sources of Optical Loss," *Journal of Endourology*, vol. 31, pp. 327–333, 1 2017.

[4] J. Marescaux and L. Soler, "Image-Guided Robotic Surgery," *Seminars in Laparoscopic Surgery*, vol. 11, pp. 113–122, 6 2004.

[5] R. Hao, O. Özgüner, and M. C. Çavuşoğlu, "Vision-Based Surgical Tool Pose Estimation for the da Vinci® Robotic Surgical System," *IEEE International Conference on Intelligent Robots and Systems*, pp. 1298–1305, 12 2018.

[6] Y. Wang, W. Ding, and D. Mei, "Development of flexible tactile sensor for the envelop of curved robotic hand finger in grasping force sensing," *Measurement*, vol. 180, p. 109524, 8 2021.

[7] D. Bouget, M. Allan, D. Stoyanov, and P. Jannin, "Vision-based and marker-less surgical tool detection and tracking: a review of the literature," *Medical Image Analysis*, vol. 35, pp. 633–654, 1 2017.

[8] E. M. Boctor, M. A. Choti, E. C. Burdette, and R. J. Webster, "Three-dimensional ultrasound-guided robotic needle placement: an experimental evaluation," *The international journal of medical robotics + computer assisted surgery : MRCAS*, vol. 4, p. 180, 6 2008.

[9] Q. Zhang, X.-G. Han, Y.-F. Xu, M.-X. Fan, J.-W. Zhao, Y.-J. Liu, D. He, and W. Tian, "Robotic navigation during spine surgery," *Expert Review of Medical Devices*, vol. 17, pp. 27–32, 1 2020.

[10] L. M. Su, B. P. Vagvolgyi, R. Agarwal, C. E. Reiley, R. H. Taylor, and G. D. Hager, "Augmented Reality During Robot-assisted Laparoscopic Partial Nephrectomy: Toward Real-Time 3D-CT to Stereoscopic Video Registration," *Urology*, vol. 73, no. 4, pp. 896–900, 2009.

[11] W. B. Shingleton and P. E. Sewell, "Percutaneous renal tumor cryoablation with magnetic resonance imaging guidance," *Journal of Urology*, vol. 165, no. 3, pp. 773–776, 2001.

[12] M. Baumhauer, M. Feuerstein, H. P. Meinzer, and J. Rassweiler, "Navigation in Endoscopic Soft Tissue Surgery: Perspectives and Limitations," *https://home.liebertpub.com/end*, vol. 22, pp. 751–766, 4 2008.

[13] R. Zhang, P.-S. Tsai, J. Cryer, and M. Shah, "Shape from Shading: A Survey," *IEEE Transactions on Pattern Analysis and Machine Intelligence*, vol. 21, pp. 690–706, 8 1999.

[14] K. Cleary and T. M. Peters, "Image-Guided Interventions: Technology Review and Clinical Applications," *Annual Review of Biomedical Engineering*, vol. 12, pp. 119–142, 7 2010.

[15] V. Lahanas, C. Loukas, and E. Georgiou, "A simple sensor calibration technique for estimating the 3D pose of endoscopic instruments," *Surgical Endoscopy*, vol. 30, pp. 1198–1204, 3 2016.

[16] A. M. Franz, T. Haidegger, W. Birkfellner, K. Cleary, T. M. Peters, and L. Maier-Hein, "Electromagnetic tracking in medicine -A review of technology, validation, and applications," *IEEE Transactions on Medical Imaging*, vol. 33, no. 8, pp. 1702–1725, 2014.

[17] M. P. Fried, J. Kleefield, H. Gopal, E. Reardon, B. T. Ho, and F. A. Kuhn, "Image-guided endoscopic surgery: results of accuracy and performance in a multicenter clinical study using an electromagnetic tracking system. 1997," *The Laryngoscope*, vol. 125, pp. 774–781, 4 2015.

[18] R. Elfring, M. De La Fuente, and K. Radermacher, "Assessment of optical localizer accuracy for computer aided surgery systems," *Computer aided surgery : official journal of the International Society for Computer Aided Surgery*, vol. 15, pp. 1–12, 2 2010.

[19] A. Reiter, P. K. Allen, T. Zhao, A. Reiter, P. K. Allen, and T. Zhao, "Articulated Surgical Tool Detection Using Virtually-Rendered Templates,"

[20] A. Sorriento, M. B. Porfido, S. Mazzoleni, G. Calvosa, M. Tenucci, G. Ciuti, and P. Dario, "Optical and Electromagnetic Tracking Systems for Biomedical Applications: A Critical Review on Potentialities and Limitations," *IEEE Reviews in Biomedical Engineering*, vol. 13, pp. 212–232, 2020.

[21] F. Bianchi, A. Masaracchia, E. Shojaei Barjuei, A. Menciassi, A. Arezzo, A. Koulaouzidis, D. Stoyanov, P. Dario, and G. Ciuti, "Localization strategies for robotic endoscopic capsules: a review," *Expert Review of Medical Devices*, vol. 16, pp. 381–403, 5 2019.

[22] L. Ma, Z. Zhao, B. Zhang, W. Jiang, L. Fu, X. Zhang, and H. Liao, "Three-dimensional augmented reality surgical navigation with hybrid optical and electromagnetic tracking for distal intramedullary nail interlocking," *The International Journal of Medical Robotics and Computer Assisted Surgery*, vol. 14, p. e1909, 8 2018.

[23] X. Liu, W. Plishker, and R. Shekhar, "Hybrid electromagnetic-ArUco tracking of laparoscopic ultrasound transducer in laparoscopic video," *https://doi.org/10.1117/1.JMI.8.1.015001*, vol. 8, p. 015001, 2 2021.

[24] A. Bajo and N. Simaan, "Kinematics-based detection and localization of contacts along multisegment continuum robots," *IEEE Transactions on Robotics*, vol. 28, pp. 291–302, 4 2012.

[25] Y. H. Su, K. Huang, and B. Hannaford, "Real-time vision-based surgical tool segmentation with robot kinematics prior," *2018 International Symposium on Medical Robotics, ISMR 2018*, vol. 2018-January, pp. 1–6, 4 2018.

[26] Y. Li, F. Richter, J. Lu, E. K. Funk, R. K. Orosco, J. Zhu, and M. C. Yip, "Super: A surgical perception framework for endoscopic tissue manipulation with surgical robotics," *IEEE Robotics and Automation Letters*, vol. 5, pp. 2294–2301, 4 2020.

[27] C. Shi, X. Luo, P. Qi, T. Li, S. Song, Z. Najdovski, T. Fukuda, and H. Ren, "Shape Sensing Techniques for Continuum Robots in Minimally Invasive Surgery: A Survey," *IEEE transactions on biomedical engineering*, vol. 64, pp. 1665–1678, 8 2017.

[28] Q. M. B. de Ruiter, F. L. Moll, and J. A. van Herwaarden, "Current state in tracking and robotic navigation systems for application in endovascular aortic aneurysm repair," *Journal of Vascular Surgery*, vol. 61, pp. 256–264, 1 2015.

[29] H. Zhao, J. Jalving, R. Huang, R. Knepper, A. Ruina, and R. Shepherd, "A helping hand: Soft orthosis with integrated optical strain sensors and EMG control," *IEEE Robotics and Automation Magazine*, vol. 23, pp. 55–64, 9 2016.

[30] S. Sareh, Y. Noh, M. Li, T. Ranzani, H. Liu, K. Althoefer, C. Harvard, and J. A. Paulson, "Macrobend optical sensing for pose measurement in soft robot arms,"

[31] S. J. Mathews, D. I. Shakir, C. A. Mosse, W. Xia, E. Z. Zhang, P. C. Beard, S. J. West, A. L. David, S. Ourselin, T. Vercauteren, and A. Desjardins, "Ultrasonic Needle Tracking with Dynamic Electronic Focusing," *Ultrasound in Medicine & Biology*, vol. 48, no. 3, pp. 520–529, 2022.

[32] J. A. van Herwaarden, M. M. Jansen, E.-j. P. A. Vonken, T. Bloemert-Tuin, R. W. M. Bullens, G. J. de Borst, and C. E. V. B. Hazenberg, "First in Human Clinical Feasibility Study of Endovascular Navigation with Fiber Optic RealShape (FORS) Technology," *European Journal of Vascular and Endovascular Surgery*, vol. 61, no. 2, pp. 317–325, 2021.

[33] A. Ebrahimi, F. Alambeigi, S. Sefati, N. Patel, C. He, P. Gehlbach, and I. Iordachita, "Stochastic Force-Based Insertion Depth and Tip Position Estimations of Flexible FBG-Equipped Instruments in Robotic Retinal Surgery," *IEEE/ASME Transactions on Mechatronics*, vol. 26, pp. 1512–1523, 6 2021.

[34] Y. Chitalia, N. J. Deaton, S. Jeong, N. Rahman, and J. P. Desai, "Towards FBG-Based Shape Sensing for Micro-Scale and Meso-Scale Continuum Robots with Large Deflection," *IEEE Robotics and Automation Letters*, vol. 5, pp. 1712–1719, 4 2020.

[35] T. Li, C. Shi, and H. Ren, "A High-Sensitivity Tactile Sensor Array Based on Fiber Bragg Grating Sensing for Tissue Palpation in Minimally Invasive Surgery," *IEEE/ASME Transactions on Mechatronics*, vol. 23, pp. 2306–2315, 10 2018.

[36] C. Lv, S. Wang, and C. Shi, "A High-Precision and Miniature Fiber Bragg Grating-Based Force Sensor for Tissue Palpation During Minimally Invasive Surgery," *Annals of Biomedical Engineering*, vol. 48, pp. 669–681, 2 2020.

[37] M. Runciman, A. Darzi, and G. P. Mylonas, "Soft Robotics in Minimally Invasive Surgery," *Soft Robotics*, 2019.

[38] A. Stilli, E. Dimitrakakis, C. D'ettorre, M. Tran, and D. Stoyanov, "Pneumatically Attachable Flexible Rails for Track-Guided Ultrasound Scanning in Robotic-Assisted Partial Nephrectomy - A Preliminary Design Study," *IEEE Robotics and Automation Letters*, vol. 4, no. 2, pp. 1208–1215, 2019.

[39] C. Wang, C. Komninos, S. Andersen, C. D'Ettorre, G. Dwyer, E. Maneas, P. Edwards, A. Desjardins, A. Stilli, and D. Stoyanov, "Ultrasound 3D reconstruction of malignant masses in robotic-assisted partial nephrectomy using the PAF rail system: a comparison study," *International Journal of Computer Assisted Radiology and Surgery*, vol. 15, pp. 1147–1155, 7 2020.

[40] "The da Vinci Research Kit (dVRK) – Intuitive Foundation."

[41] C. D'Ettorre, A. Mariani, A. Stilli, F. Rodriguez Y Baena, P. Valdastri, A. Deguet, P. Kazanzides, R. H. Taylor, G. S. Fischer, S. P. Dimaio, A. Menciassi, and D. Stoyanov, "Accelerating Surgical Robotics Research: A Review of 10 Years with the da Vinci Research Kit," *IEEE Robotics and Automation Magazine*, vol. 28, pp. 56–78, 12 2021.

[42] A. Méndez and F. Bragg, "Fiber Bragg grating sensors: a market overview," *https://doi.org/10.1117/12.738334*, vol. 6619, pp. 44–49, 7 2007.